Tomographic filtering of shear and compressional wave models reveals uncorrelated variations in the lowermost mantle

Jun Su [1,2] Christine Houser,[1] John W. Hernlund[1,2] and Frédéric Deschamps[3]

[1]*Earth-Life Science Institute, Tokyo Institute of Technology, Tokyo* 152-8551*, Japan. E-mail:* junsu@elsi.jp
[2]*Department of Earth and Planetary Science, Tokyo Institute of Technology, Tokyo* 152-8551*, Japan*
[3]*Institute of Earth Sciences, Academia Sinica, Taipei* 11529*, Taiwan*

SUMMARY

Seismic tomography models reveal differences in the geographic distribution and magnitude of *P*- and *S*-wave velocity variations (V_P and V_S, respectively) below $\sim$2200 km depth in the Earth's mantle. In particular, large low shear velocity provinces (LLSVPs) beneath the Pacific and Africa exhibit a distinct low velocity population in the distribution of V_S that does not stand out in V_P models, carrying important implications for the origin of these features. However, it is possible that the absence of a distinct low velocity feature in V_P models is an artefact of V_P models having lower resolution compared to V_S models owing to differences in coverage. Here, we use 'tomographic filters' computed from the singular value decomposition of the sensitivity matrices for a pair of V_P and V_S models in order to test whether such low velocity features are suppressed in V_P models. Our 'cross-filtered' results show that resolution alone cannot explain the absence of a corresponding low V_P population. We additionally apply the joint V_P and V_S tomographic filter technique to thermochemical mantle convection models to show that cases with distinct phase and/or composition may be differentiated from cases where only temperature varies. We then develop a new proxy for exploring uncorrelated V_P and V_S more broadly using the difference between the observed V_P model and the filtered V_S model input. Our results show that 'large uncorrelated modulus provinces' (LUMPs) extend beyond the boundaries of LLSVPs, and exhibit anomalies in both fast and slow regions.

Key words: Composition and structure of the mantle; Inverse theory; Statistical methods; Seismic tomography.

1 INTRODUCTION

Two distinct kinds of elastic waves propagate in the rocky mantle: *P* (compressional) and *S* (shear). Measurements of the propagation speeds, V_P and V_S (respectively), offer unique windows into lower mantle rock properties owing to their different dependence on elastic moduli. In particular, $\rho V_P^2 = K + 4\mu/3$ while $\rho V_S^2 = \mu$, where ρ is the density, K the bulk modulus and μ the shear modulus. To first order, variations in μ and K that are driven by variation of a single parameter (such as temperature) will give rise to correlated variations in V_P and V_S (i.e. $\delta\log V_P \propto \delta\log V_S$; hereafter, $\delta\log V$ is denoted as δV for brevity). A lack of such a correlation and/or a change in their proportionality implies that additional parameters may be influencing the elastic moduli, such as changes in phase and/or chemical composition. For this reason, the determination of distinct V_P and V_S variations in the Earth's interior has become a key target for diagnosing the nature of heterogeneity inside our planet, with implications for long-term dynamics and evolution. While the use of V_S tomography models for such interpretations is common, relatively few studies have considered both V_P and V_S tomographic

models for direct comparison with hypothesized dynamic scenarios (e.g. Simmons *et al.* 2010; Koelemeijer *et al.* 2016, 2018; Lei *et al.* 2020).

In the lowermost mantle, the so-called large low shear velocity provinces (LLSVPs) below Africa and the Pacific (Hernlund & McNamara 2015) are prominent features of V_S tomography models (Becker & Boschi 2002; Trampert *et al.* 2004; Trønnes 2009; Cottaar & Lekic 2016), and have inspired many ideas about their role in Earth's history. These features have been interpreted as super/megaplumes (Matyska *et al.* 1994; Thompson & Tackley 1998; Davaille 1999; Jellinek & Manga 2004; Maruyama *et al.* 2007; Burke *et al.* 2008; Hassan *et al.* 2020) and/or compositionally distinct chemical piles (Kellogg *et al.* 1999; McNamara & Zhong 2005; Tan & Gurnis 2007; Ohta *et al.* 2008; Deschamps *et al.* 2012; Jones *et al.* 2020), and may be related to early differentiation events (Walter & Trønnes 2004; Labrosse *et al.* 2007; Wang *et al.* 2013; Trønnes *et al.* 2019; Wang *et al.* 2021), a 'slab graveyard' of basaltic crust (Christensen & Hofmann 1994; Tackley 2011; Jones *et al.* 2021), and have even been linked to mass extinction events (Richards *et al.* 1989; Courtillot 2002; Isozaki 2009).

V_P tomography models, on the other hand, reveal only moderately slow anomalies in the same regions when compared to V_S (Fig. 1). Previous studies (Karato & Karki 2001; Simmons *et al.* 2010; Della Mora *et al.* 2011; Koelemeijer *et al.* 2016; Tesoniero *et al.* 2016; Chaves *et al.* 2021) compared the seismic ratio $R_{S/P} = \delta V_S/\delta V_P$ at different depths and reported an increase of $R_{S/P}$ from smaller than 2.5 to larger than 3 in the lowermost mantle with increasing depth, motivating explanations involving the contribution of factors other than temperature variations alone (Deschamps & Trampert 2003; Brodholt *et al.* 2007). However, $R_{S/P}$ is only a measure of amplitude ratio of apparently correlated δV_P and δV_S, and does not by itself reveal the quality of the correlation nor the underlying reasons for changes in $R_{S/P}$. Key details of the relative differences are revealed by plotting the distribution of δV_P and δV_S in tomographic models at each depth (e.g. Hernlund & Houser 2008, fig. 1), in which a distinct low velocity population appears in V_S models below 2200 km depth that is not apparent in V_P models. Because this change occurs over a depth/pressure range greater than can be explained by variations in the high pressure phase post-perovskite (pPv, Hirose 2006), the distinct 'slow tail' in δV_S distribution curves and its absence in δV_P has been invoked as evidence of chemical composition heterogeneity (Hernlund & Houser 2008). Note that this argument assumes that both V_P and V_S tomographic models have sufficient resolution in these slow regions to enable such a comparison. A departure from $\delta V_P \propto \delta V_S$ (i.e. 'de-correlation') is also apparent in raw traveltime residuals at turning point depths in these regions (Bolton & Masters 2001; Chaves *et al.* 2021), without performing any tomographic inversion. Normal mode observations, which are not *a priori* affected by the same kinds of relative resolution issues as traveltime tomography, initially supported the presence of these uncorrelated velocity variations (Ishii & Tromp 1999; Trampert *et al.* 2004). However, recent studies using newer data suggest that δV_P and δV_S are more correlated (Moulik & Ekström 2016; Koelemeijer *et al.* 2016), and thus may not require a distinct composition within LLSVP.

Three possibilities have been considered to explain the lack of a corresponding low V_P population like the one seen in V_S models: (1) a relative dearth of coverage/resolution in V_P models (Davies *et al.* 2012, 2015) without core-reflected P phases and which previously lacked diffracted P phases, (2) the measured traveltime delay of P waves propagating through these regions is dampened by a combination of wavefront healing effects and traveltime picking artefacts (Schuberth *et al.* 2009; Malcolm & Trampert 2011) and/or influence of upper-mantle structure where most ray paths resolving the region come from close source–receiver pairs (Chaves *et al.* 2021), or (3) changes in rock properties that manifest differently for V_P and V_S (Kellogg *et al.* 1999; Trampert *et al.* 2004; Simmons *et al.* 2007; Hernlund & Houser 2008). If (1) or (2) are the dominant factors and V_P is found to behave similarly to V_S in the real Earth, then the Pacific and Africa features may be inclusively called LLVP (Koelemeijer *et al.* 2018), as opposed to LLSVP. However, it remains to be demonstrated that a lack of resolution is able to explain the absence of these pronounced low velocity features in many P models similar to those obtained in S models.

In this study, we consider the possibility of an inherent resolution difference by employing the method of 'tomographic filtering' using a pair of V_P and V_S models (Houser *et al.* 2008). We apply the same procedure and parameters to perform the inversion, in order to test whether relatively poor coverage in P waves explains the difference in V_P and V_S distribution obtained from tomographic models. Tomographic filtering has been used in several studies (e.g. Ritsema *et al.* 2007; Della Mora *et al.* 2011; Davies *et al.* 2012; Koelemeijer *et al.* 2018; Simmons *et al.* 2019) to assess the consistency

of hypothesized seismic velocity structures with features in tomographic models. In this method, a 'resolution matrix' (or resolution operator, Ritsema *et al.* 2007) is formed by computing the product of the pseudo-inverse of the sensitivity matrix with the sensitivity matrix itself. The resolution matrix would be equal to the identity matrix in the ideal case, however, owing to heterogeneous coverage and regularization the resolution operator is not unity in practice. By applying the resolution matrix to hypothetical seismic velocity structures, one obtains a 'filtered' version of seismic velocity structure as it would be rendered by the tomographic inversion. As such, the tomographic filter is a useful tool to address questions related to relative resolution between different models, and to evaluate the consistency between hypothesized seismological structures in the Earth and those observed in tomographic models.

Here we introduce a 'cross-filtering' technique by applying the V_P tomographic filter to the δV_S model, and vice versa for the V_S filter and δV_P model. We find that a slow tail would be resolved in the V_P models if it were present in the real mantle, and therefore its absence in V_P tomography models cannot be explained by resolution alone. We then apply our joint V_P and V_S filters to thermo-chemical models of mantle convection to examine the influence of filtering on inferences of variations in temperature, composition, and phase, and find that variations in both chemical composition and pPv are helpful in explaining the discrepancy between V_P and V_S tomography models. Finally, we define a new variable, denoted as $\Delta \bar{V}$, to assess the geographic distribution of uncorrelated cross-filtered δV_P and δV_S more broadly. Our global mapping of uncorrelated variations reveals that such anomalies are not confined to LLSVPs alone and appear to be a more ubiquitous feature of the deep mantle that merits further study.

2 METHODS

Here we outline our methods, including our choice of tomographic models, statistical characterization, construction of tomographic resolution operators and application to filtering geodynamic models.

2.1 Tomography models

The seismic data and parametrization of this study are inherited from the HMSL-P06 and HMSL-S06 models (Houser *et al.* 2008), consisting of 252 426 *S*-wave (*S*, *SS*, *SS-S* and *ScS-S*) 251 617 *P*-wave (*P*, *PP* and *PP-P*) traveltime measurements along with surface wave data. The two models adopt the same approaches for data curation, phase picking, regularization and inversion, allowing for a more robust comparison than model pairs that are constructed using different methodologies. The Earth's mantle is modeled with 18 layers of equal-area blocks with $4°$ width at the equator, and the layers in the lower mantle have an equal thickness (200 km), with the total model consisting of 46 404 blocks. See Houser *et al.* (2008) for further details on the model construction.

Because this study focuses on relative resolution of *P*- and *S*-wave coverage in the lower mantle, we use only the sensitivity kernels for 36 092 blocks in the lower mantle and transition zone to obtain resolution operators (see below). Thus, the resolution analysis we demonstrate here does not include the influence of upper-mantle structure and travel time (including surface wave) uncertainty, although these factors are considered in tomographic models obtained in the original Houser *et al.* (2008) study and in Supporting Information S.1 of this study where we show models
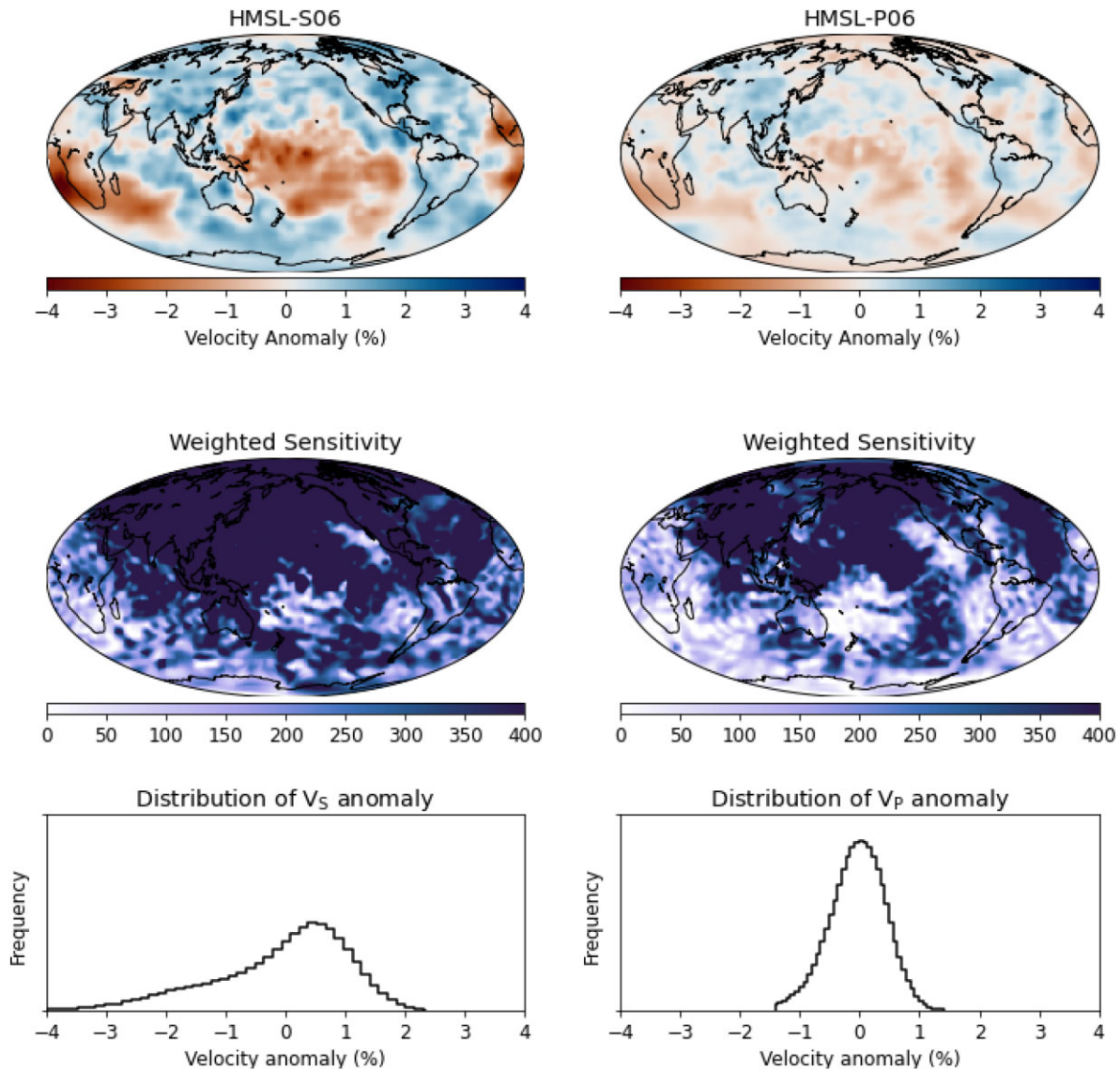
Figure 1. Tomographic models (top), geographic coverage as measured by weighted sensitivity (middle), and distribution of seismic velocities in the lowermost mantle bottom layer at 2800 km depth for δV_S (left) and δV_P (right) of Houser *et al.* (2008). Models are plotted using the same coloúr scale in order to emphasize their differences. The Pacific hemisphere (centred at 180°) comprises ≈52 per cent of the slow tail ($\delta V_S < -1$ per cent), only slightly larger than the African hemisphere (centred at 0°).

for comparison. The HMSL models use ray theory to track *P* and *S* waves through the mantle, and thus result in a sparse sensitivity matrix which is ideal for matrix decomposition. The HMSL-P06 and HMSL-S06 models include data up to 2005, and contain less data than more recent models. The sparseness and smaller size of our sensitivity matrix enables a full analysis to be computationally tractable. Note that the use of models containing fewer data will not affect the conclusions of our study, as they represent a lower bound on resolution.

2.2 Resolution operator

The resolution operator **R** expresses the smoothing and damping effects caused by a particular tomographic inversion. Tomographic inversions for seismic velocity typically assume a linear relation between the travel time observation and discretized model velocity perturbations through which seismic waves propagate. This relation

is written in matrix form as:

$$\mathbf{Gm} = \mathbf{d}, \tag{1}$$

where **m** is the discretized model, **d** is the traveltime data and **G** is the sensitivity matrix whose rows are comprised of kernels constructed for each source–receiver pair in the data set.

An approximate solution for **m** (in the least-squares sense) can be obtained by finding a 'generalized' or 'pseudo-inverse' $\mathbf{G}^\dagger$ and multiplying it with **d** as follows:

$$\mathbf{m}^\dagger = \mathbf{G}^\dagger \mathbf{d} = \mathbf{G}^\dagger \mathbf{Gm} = \mathbf{Rm}, \tag{2}$$

where $\mathbf{m}^\dagger$ is the regularized model and $\mathbf{R} = \mathbf{G}^\dagger \mathbf{G}$ is the 'resolution operator'. In the ideal case $\mathbf{R} = \mathbf{I}$ (the identity matrix) and $\mathbf{m}^\dagger = \mathbf{m}$. However, owing to heterogeneous coverage of seismic waves resulting in an uneven density of **G** in addition to regularization (damping), in practice we ordinarily have $\mathbf{R} \neq \mathbf{I}$ and, as a result, $\mathbf{m}^\dagger \neq \mathbf{m}$. By applying the resolution operator **R** to any hypothetical

model $\mathbf{m_h}$, one obtains the 'filtered model' $\mathbf{m_h}^\dagger = \mathbf{Rm_h}$ as it would be rendered by the tomographic inversion (Ritsema *et al.* 2007).

Here', we utilize the singular value decomposition (SVD) method to obtain $\mathbf{R}$ for the HMSL-P06 and HMSL-S06 models. The sensitivity matrix $\mathbf{G}$ is decomposed as:

$$\mathbf{G} = \mathbf{U\Sigma V^T}, \tag{3}$$

where $\mathbf{\Sigma}$ is the matrix with the singular values $\mathbf{s}$ on its diagonal ($\mathbf{\Sigma} = \mathrm{diag}(\mathbf{s})$), $\mathbf{U}$ is a matrix containing the left singular vectors and $\mathbf{V}$ hosts the right singular vectors. Since $\mathbf{U}$ and $\mathbf{V}$ are orthonormal matrices, an estimated inverse of $\mathbf{G}$, or $\mathbf{G}^\dagger$, is obtained as:

$$\mathbf{G}^\dagger \approx \mathbf{VLZU}^T, \tag{4}$$

where $\mathbf{Z}$ is an approximate inverse of the diagonal matrix $\mathbf{\Sigma} = \mathrm{diag}(1/\mathbf{s})$ and $\mathbf{L}$ is the regularization operator. Note that this kind of regularization is different from the original approach used to construct HMSL-P06 and HMSL-S06, which applied roughness damping as additional terms in $\mathbf{G}$ itself.

The SVD inversion above becomes unstable for small singular values, however, these represent unimportant contributions to the inversion and are damped (e.g. Ritsema *et al.* 2007, with a global damping factor ϵ) or truncated in practice (i.e. $1/\mathbf{s}$ is set as 0 for $s < s_{\min}$, where $s_{\min}$ is a cut-off value). Here, we retain the largest 6000 out of 36 092 singular values and truncate the remainder to avoid overfitting (Supporting Information S.1). With this $\mathbf{G}^\dagger$ reconstructed, we can write the resolution operator as:

$$\mathbf{R} = \mathbf{G}^\dagger \mathbf{G} \approx \mathbf{VLZU}^T \mathbf{G}. \tag{5}$$

Using this approximation, we calculate $\mathbf{R}$ for both the δV_P and δV_S models, denoted as R_P and R_S, respectively. A filtered model is the product of R_P or R_S with the original model values. For example, the δV_S model cross-filtered by our P model resolution operator is simply $R_P \delta V_S$. This estimation of $\mathbf{R}$ does not involve traveltime data $\mathbf{d}$, and thus the quality of the data has no influence on $\mathbf{R}$ nor the cross-filtering technique. The SVD inversion model ($\mathbf{m}^\dagger = \mathbf{G}^\dagger \mathbf{d}$) may differ from a model constructed from other methods such as the least-squares approach used for the HMSL models. Differences in the models can arise because the kernel used in our analysis is a subset of the original HMSL model kernel, and the regularization schemes are not the same since it is not straightforward to apply roughness damping when using SVD. Thus, here we do not argue for any advantage of SVD for creating tomographic models, but rather to demonstrate how SVD provides tools to interrogate and compare tomography models.

For the above computations, we utilized the super-computer TSUBAME3.0 at the Tokyo Institute of Technology to obtain the SVD of the sensitivity matrices $\mathbf{G}$ and the reconstruction of resolution operators $\mathbf{R}$. We utilized the parallel algorithms in the software package ScaLAPACK (Blackford *et al.* 1997). Optimized by Intel C/C++ and FORTRAN compilers, the entire calculation requires $\sim$2000 core-hours to complete for the present models.

2.3 Statistical analysis

Previous studies (Yanagisawa & Hamano 1999; Hernlund & Houser 2008) have identified Gaussian-like distribution patterns in velocity variations extracted from tomography models by analysing the areal abundance $f(V)$ (i.e. frequency per unit solid angle coverage) over anomaly amplitude at each depth in the model domain(s). We follow the same approach to construct distributions from frequency histograms of velocity amplitude at each depth as Hernlund

& Houser (2008), and apply Gaussian least-squares fitting to the distributions for the tomographic-filtered velocity anomaly $R\delta V$ around their dominant modes. We search for the dominant mode peak at the maximum frequency M with standard deviation σ using an iterative fitting procedure that provides the best fit of the Gaussian curve in the range $M - \sigma \leq R\delta V \leq M + \sigma$. Additionally, a diffusion damping is equally applied to the classified bins in all histograms to smooth sharp variations and provide a more robust fit. This adjustment makes little change in the observation (cf. Fig. 1 of this study and fig. 1 of Hernlund & Houser 2008) where distributions are initially Gaussian-like, but it facilitates the fitting of distributions derived from synthetic models in which the amplitude of adjacent bins changes more dramatically owing to aliasing effects. Note that the treatment is only used to obtain parameters pertaining to characterization of the distributions (i.e. M and σ); the values of velocity perturbations used in other computations are not affected.

To compare distributions for filtered results of δV_P and δV_S we align the dominant modes (M_P and M_S) as a common point of reference and scale the amplitude of δV_P by σ_S / σ_P using the following linear transformation:

$$R_S \delta \bar{V}_P = \frac{\sigma_S}{\sigma_P}(R_S \delta V_P - M_P) + M_S \tag{6}$$

where $R_S \delta \bar{V}_P$ is the normalized relative seismic velocity amplitude with the filtered S model ($R_P \delta V_S$) with mode M_S and variance σ_S. Normalization of the amplitude of δV_P variations to match those of δV_S models facilitates quantitative comparisons. With $R_S \delta \bar{V}_P$ obtained by eq. (6) we can take the difference between cross-filtered model pairs to estimate a resolution-filtered discrepancy between δV_P and δV_S models:

$$\Delta \bar{V} = R_S \delta \bar{V}_P - R_P \delta V_S. \tag{7}$$

This will be used in our later exploration of more general uncorrelated moduli in the lower mantle (i.e. not limited to LLSVPs).

Our above procedures additionally enable an estimate of the volume of material for which $R_P \delta V_S$ does not vary in proportion to $R_S \bar{V}_P$, which we simply define as X_{het}:

$$X_{\text{het}} = \int_{-\infty}^{M} \left[f(R_P \delta V_S) - f\left(R_S \delta \bar{V}_P\right) \right] \mathrm{d}V \tag{8}$$

X_{het} can be evaluated at a single depth or integrated over a range of depths. The same calculation can be carried out for fast velocities ($V > M$), however, in this study we focus on slow velocities ($V < M$).

2.4 Method for filtering geodynamic models

We additionally apply tomographic filters to geodynamic model outcomes of convection simulations and conduct the same statistical analysis as described above in order to assess potential contributions of chemical composition and phase heterogeneity. Here, we follow recent studies (Deschamps *et al.* 2018; Deschamps & Li 2019) and consider a compositionally layered lower mantle, consisting of a dense (3 per cent enriched in iron and 18 per cent in bridgmanite) 'primordial' material occupying 3.5 per cent of the total mantle volume at the bottom for TC4 and TC4-pPv (Table 1). We refer the reader to table 2 of Deschamps *et al.* (2018) for detailed geodynamic parameters. Two models (T1-pPv and TC4-pPv) include the pPv phase change at the bottom of the mantle. In these cases, the Clapeyron slope and CMB temperature are fixed to $\Gamma = 13$ MPa K^{-1} and $T_{\text{CMB}} = 3750$ K, respectively. The pPv phase is

Table 1. Key parameters for convection models T1, T1-pPv, TC4 and TC4-pPv from Deschamps *et al.* (2018). A pPv phase transition is included in T1-pPv and TC4-pPv and dense primordial material in TC4 and TC4-pPv.

Parameter		T1	T1-pPv	TC4	TC4-pPv
Clapeyron slope of post-perovskite	(Γ)	–	13 MPa K^{-1}	–	13 MPa K^{-1}
Post-perovskite velocity jump	($\Delta\rho_{pPv}$)	–	62 kg m^{-3}	–	62 kg m^{-3}
Volume fraction of dense material	(X_{prim})	–	–	3.5 per cent	3.5 per cent
Buoyancy ratio	(B_Z)	–	–	0.15	0.15
Compositional viscosity ratio	($\Delta\eta_C$)	–	–	30	30
Logarithmic thermal viscosity ratio	(E_a)			20.723	
CMB temperature	(T_{CMB})			3750 K	

assumed to have the same viscosity as bridgmanite, and a density excess of 62 kg m^{-3}. With these parameter values, pPv forms lens-like structures above the CMB, that is, pPv transforms back to bridgmanite a few tens of kilometres above the CMB, a structure also known as a 'double-crossing' (Hernlund *et al.* 2005). In addition, pPv is not stable within piles of hot dense material (representing the LLSVPs). Note that for values of Γ and/or T_{CMB} lower than those in T1-pPv and TC4-pPv, pPv patches may be present within LLSVPs, as observed by other simulations (Li *et al.* 2016). However, even in this case, pPv patches are thin (a few tens of kilometres in thickness) and small. Their seismic signatures would thus be diluted and have no or very limited impact on the synthetic (i.e. calculated from the numerical simulations temperature, composition and phase fields) shear velocity anomalies averaged out over the lowermost 200 km. Geodynamic models produce (non-dimensional) thermal and compositional fields, which can be converted into seismic velocity anomalies. We follow the method described in the Supporting Information of Deschamps & Li (2019), to which we refer for further details. We then project these synthetic seismic velocities to the parametrization of the HMSL models and downsample them using simple averaging before applying the corresponding *P*- and *S*-wave resolution operators. The projection is applied to all four geodynamic models twelve times, each rotated by different angles based on the 12 vertices of an icosahedron, to examine the influence of uneven geographical sensitivity of the resolution operators (Supporting Information S.2). The volume fraction and X_{het} are estimated by the average of all rotated models, however, for brevity we show distribution curves for rotation results from only one of the angles in the results (see the Supporting Information for an exploration/comparison of all angles).

3 RESULTS

Here, we describe our results obtained in two different kinds of applications: (1) comparing *S*-wave structure filtered by the *P*-wave resolution operator to *P*-wave structure filtered by the *S*-wave resolution operator, also known as 'cross-filtering', and (2) measuring heterogeneous fraction X_{het} in tomographically filtered δV_P and δV_S obtained from the geodynamic models T1, T1-pPv, TC4 and TC4-pPv.

3.1 Cross-filtering

We synthesized hypothetical models $R_S\delta V_P$ and $R_P\delta V_S$ by filtering the δV_S model using the *P*-wave resolution matrix R_P, and vice versa, respectively. The distributions of velocity anomalies for the cross-filtered results are shown in Fig. 2 with the original models as a reference. The increasing negative skewness of distributions below

2200 km is confined to the δV_S model and the *P*-filtered δV_S model ($R_P\delta V_S$). Such a component reveals a non-Gaussian distribution that deviates from the dominant mode, whereas curves for δV_P and $R_S\delta V_P$ are nearly symmetric and normally distributed. We treat the 'slow tail' in δV_S and $R_P\delta V_S$ as a distinct low velocity population in the distribution, rather than simply a change in the skewness of a single population. It is also noteworthy that cross-filtering decreases the amplitude of δV_S structure and renders the dominant mode more similar to δV_P, which suggests that *P* resolution does have some effect on the relatively small variance of velocity anomaly in tomographic images.

Next, we normalized $R_S\delta V_P$ to $R_P\delta V_S$ using eq. (6) for comparison and measured the fraction that deviates from Gaussian distribution X_{het}. The variation at 2800 km depth suggests a significant (X_{het} ~14 per cent) non-Gaussian component (Fig. 3) that decreases with height from the CMB. We then measure the volume fraction of the heterogeneity in the whole mantle by integrating the lowermost three layers (below 2400 km).

The results (rightmost column in Table 2) indicate that the volume fraction of heterogeneity resolved by the tomographic model is $\approx$0.94 per cent of the whole mantle. Because cross-filtering damps the amplitude of velocity structure, the volume measured here is smaller than the work of Hernlund & Houser (2008) and other tomography models which typically find the heterogeneity comprises $\approx$2 per cent of the mantle volume.

3.2 Tomographic filtering of geodynamic models

We next examine the volume fraction of thermo-chemical features by filtering geodynamic models following a similar approach we used to obtain $R_P\delta\bar{V}_P$ and $R_S\delta V_S$ (Fig. 4). First, we applied tomographic filters to a purely thermal model to validate if there is a de-correlation generated between δV_P and δV_S as a consequence of different filters/resolution operators. *P*- and *S*-wave filters are applied to the seismic velocity models derived from the geodynamic model T1, and the results suggest that no significant slow tail or peak shifts emerge in the distribution curves (Fig. 5, top left). We normalized the filtered *P*-wave result ($R_P\delta V_P$) to *S* wave ($R_S\delta V_S$) and measured the heterogeneity fraction X_{het} using the same method as above and found <0.3 vol per cent heterogeneity in the whole mantle. This volume is much smaller than the results obtained from the tomography models indicating that a small portion of the uncorrelated velocity anomalies may be generated through the process of tomographic filtering. Della Mora *et al.* (2011) measured $R_{S/P}$ of a filtered purely thermal model deduced from Nakagawa *et al.* (2009) and also found that high $R_{S/P}$ values in the lowermost mantle are not produced as an artefact of filtering.
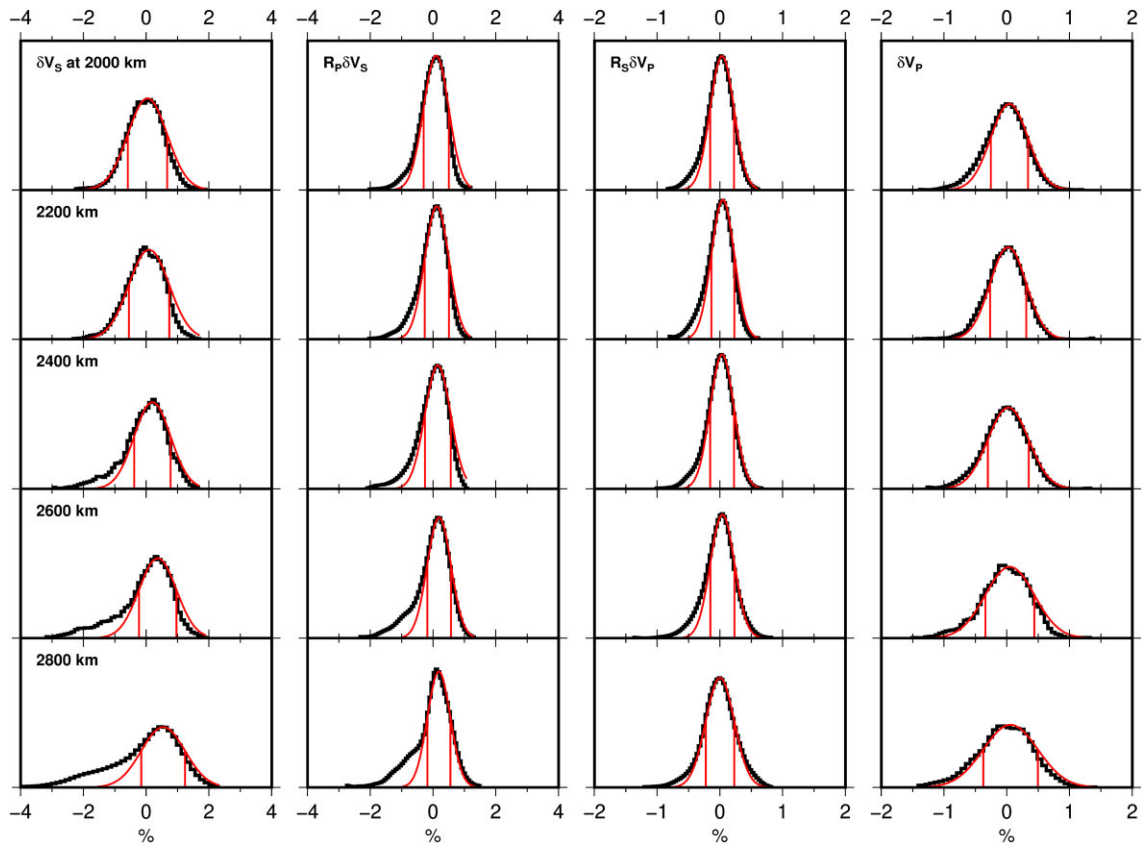
Figure 2. Histograms (black) and Gaussian fitting curves (red) for seismic anomalies in tomographic V_S (left-hand column) and V_P (right-hand column) models, and the cross-filtered results $R_P\delta V_S$ (centre-left column) and $R_S\delta V_P$ (centre-right column) derived from HMSL-P06 and HMSL-S06. The total areal abundance is normalized and the horizontal axes have different scales to facilitate comparison. The dominant modes are approximated by Gaussian-fitting shown in red curves, and the best fit $\pm\sigma$ interval in vertical lines. Contribution of the Pacific and African hemisphere in the filtered result remains at a similar and rather equal ratio, estimated by a cut-off value $R_P\delta V_S = -0.5$ per cent.

Since temperature variations in the mantle convection model do not appear to be solely responsible for the kinds of uncorrelated variations found in tomographic model pairs, we infer that an iso-chemical scenario without pPv phase transition cannot explain the seismological structure of the deep mantle. Hence, we examine the extent to which non-thermal variations, such as ancient dense iron-enriched material and/or a pPv phase transition, provide a satisfactory explanation for these uncorrelated velocity anomalies (Hirose 2006; Stackhouse *et al.* 2006).

The filtered results for TC4 (Fig. 5, top right) produce slow tails in the deepest model layers, similar to what is found in tomography models, but the slow tail also appears in the δV_P distribution and yields relatively little discrepancy between δV_P and δV_S. Although the non-zero sensitivity of V_P to Fe-enrichment in the synthetic model might be partly responsible for the slow-tail pattern in δV_P and, as a result, the underestimation of heterogeneity volume, we still follow the previous definition to evaluate the volume for consistency. Mantle convection simulations span geological timescales (billions of years), and the initial 3.5 per cent primordial material has mostly been mixed by viscous entrainment since only 0.47 per cent is measured by this analysis with the resolution derived from HMSL models. The volume of the primordial material remaining from the dynamic models is smaller than the value of 0.94 per cent obtained from the tomography models.

Next, we investigated how a pPv phase transition influences the velocity variations using filtered T1-pPv and TC4-pPv models (Fig. 5, bottom panels). pPv may be present within subducted slabs, which bring cold oceanic crust into the D″ layer (Hutko *et al.* 2006), and may be a plausible explanation for the uncorrelated variations owing to the different effects that the phase change has on δV_P and δV_S (Tsuchiya *et al.* 2004). The addition of pPv does little to change the distribution curves for T1-pPv compared to T1, except for the increased magnitude of variation of the dominant modes which remain symmetric in the D″ layer. There are no obvious slow tails from the T1-pPv model, and the measurement yields only 0.39 per cent heterogeneity. On the other hand, clear slow tails appear in both δV_P and δV_S in TC4-pPv, similar to TC4, but the inclusion of pPv causes a strong de-correlation in δV_S with a large population of slow anomalies in the lowermost 400 km. This difference results in a remarkable increase in heterogeneity volume to 1.6 per cent, which is comparable to the value of 0.94 per cent from the tomography models.

The resolvable volume of uncorrelated heterogeneity measured in the T1 model, where velocity anomalies depend only on temperature, is not comparable to those observed in tomographic models. On the other hand, models with phase change and/or chemical heterogeneity (T1-pPv, TC4 and TC4-pPv) increasingly reproduce the uncorrelated velocity variations, as shown in Table 2. It is notewor-
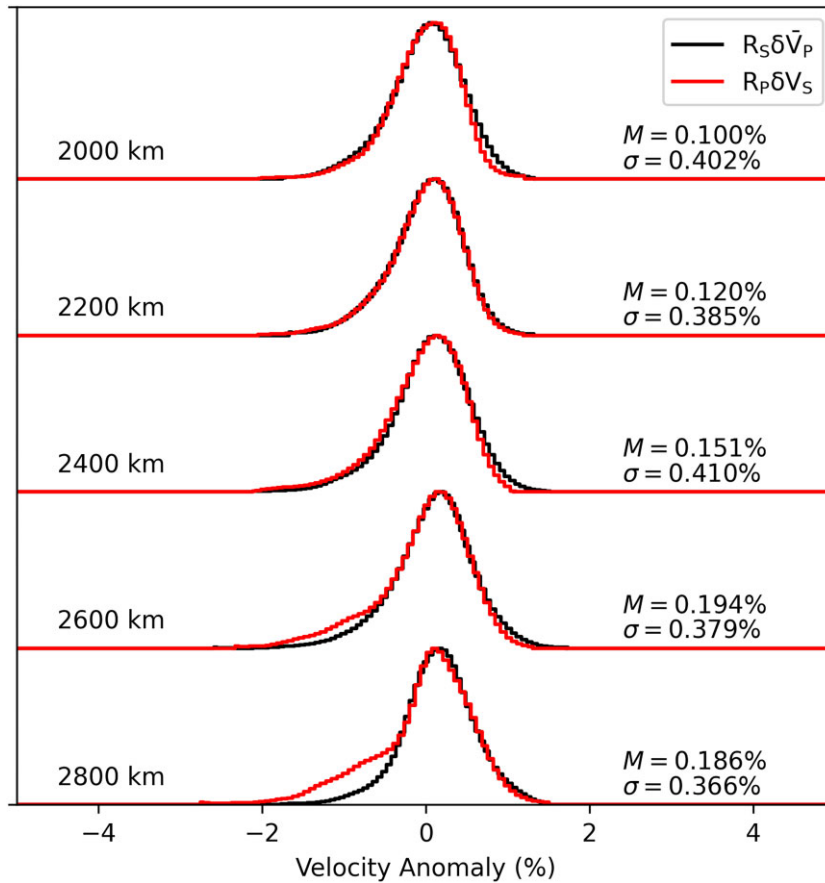
Figure 3. Distribution curves for $R_S\delta\bar{V}_P$ (black) and $R_P\delta V_S$ (red) at 2000, 2200, 2400, 2600 and 2800 km depth. M_S and σ_S are used to normalize filtered P model curves, which are aligned by dominant modes with reference to $R_P\delta V_S$. The P data are capable of resolving the slow tail from the V_S model, and the S data are capable of resolving the absence of a slow tail in the V_P model.

Table 2. The volume fraction of heterogeneity (X_{het}) in the lower mantle of the geodynamic model T1, T1-pPv, TC4, TC4-pPv and tomographic model HMSL-P06/S06. We integrate X_{het} to estimate volume of heterogeneity using the values in the same three bottom layers (in bold font). A negative fraction could suggest that $f(R\delta\bar{V}_S)$ is generally smaller than $f(R\delta\bar{V}_P)$ if the value is significant ($|X_{het}| > \sigma$).

Depth (km)	Volume fraction				
	T1	T1-pPv	TC4	TC4-pPv	Cross-filtered
735	−0.00406	0.00207	−0.00523	0.01071	0.05376
885	−0.00446	0.00037	−0.01395	−0.01219	0.00942
1035	0.00291	0.00343	−0.00752	−0.00296	0.00030
1210	0.00526	0.00982	−0.01132	−0.01121	0.00358
1400	−0.00071	0.00335	0.00179	0.00464	−0.03994
1700	0.00308	0.00634	0.00771	−0.00625	0.00549
2000	0.00602	−0.00324	0.00856	−0.00424	−0.01359
2200	0.00203	−0.00454	0.00997	0.00440	−0.00287
2400	**0.00257**	**0.01357**	**0.02083**	**0.02416**	**0.04852**
2600	**−0.01342**	**−0.01054**	**0.04284**	**0.17761**	**0.06977**
2800	**-0.07243**	**−0.09190**	**0.06448**	**0.23440**	**0.14168**
σ among layers	0.02147	0.02761	0.02296	0.08086	0.04784
Volume of heterogeneity	0.294 per cent	0.393 per cent	0.466 per cent	1.555 per cent	0.940 per cent

thy that including pPv in the thermochemical model (cf. TC4 and TC4-pPv) causes an increase in heterogeneity volume which cannot be reduced to the summation of those measured in the thermochemical model without it (TC4) and in the thermal model including it (T1-pPv).

The radial distribution of heterogeneity fraction also differs between the tomography and dynamic models. The resolved heterogeneity volume in TC4-pPv is close to the cross-filtered results and concentrated in the bottom 400 km of the mantle with a rapid drop in volume above 400 km. Whereas, the heterogeneity fraction in
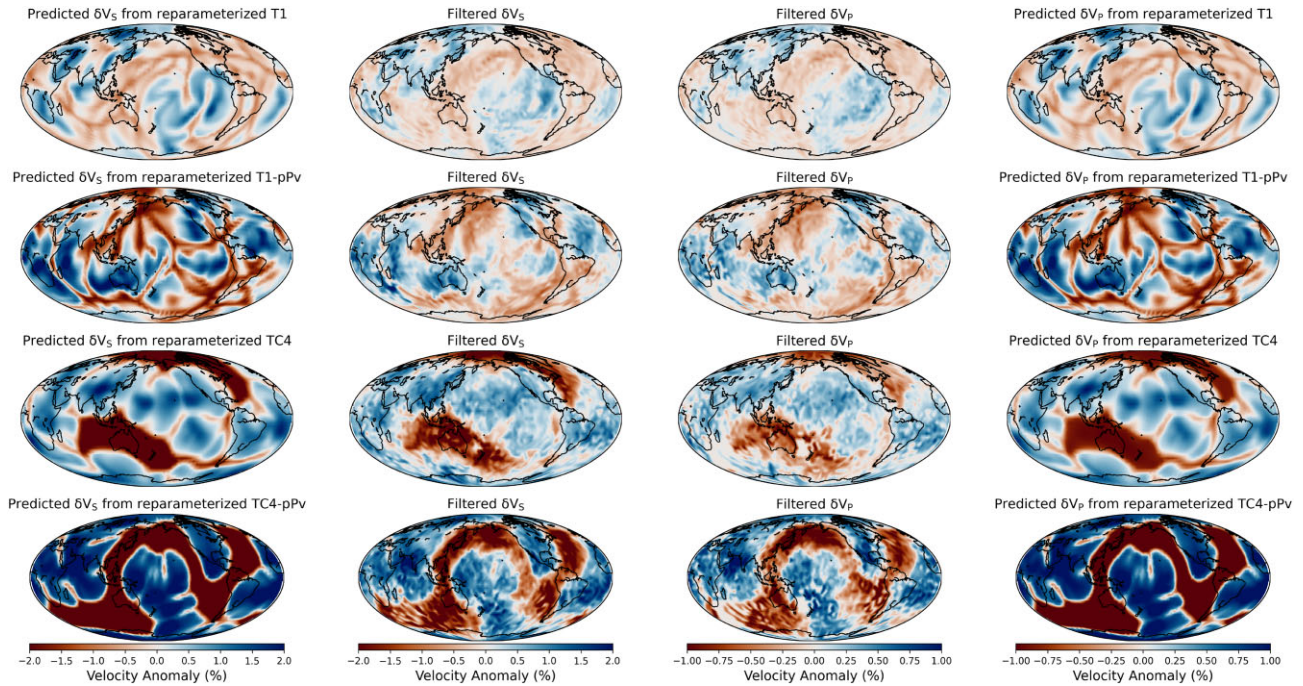
Figure 4. Filtered results for δV_P and δV_S at the 2800 km depth predicted by geodynamic model T1, T1-pPv, TC4 and TC4-pPv reparametrized and filtered by HMSL-S06 and HMSL-P06. See Table 1 for the difference in these models.

tomography models gently decreases with height above the CMB which may imply the geometry of LLSVPs in the mantle that is somewhat different than thermochemical features in the synthetic models.

4 DISCUSSION

The above results enable us to (1) assess the influence of relatively poor P model resolution on the lack of low V_P anomalies similar to those seen in V_S models, (2) examine the extent to which temperature variations alone could explain uncorrelated δV_P and δV_S in the tomographic model pair, (3) infer that the presence of additional influences (e.g. composition and/or phase) may help to explain δV_P and δV_S model differences and (4) to explore the nature and distribution of uncorrelated variations in the deep mantle after removing the influence of resolution differences and correlated variations. We discuss all of these further below.

4.1 Sufficiency of P model coverage

The non-Gaussian pattern for $R_P \delta V_S$ (Fig. 2) demonstrates that HMSL-P06 has sufficient resolution to recover the anomalously low velocity structures associated with LLSVPs to a similar extent as HMSL-S06, in spite of differences in ray coverage between the V_P and V_S models. This is the first demonstration of the relative resolving power of a V_P model compared to V_S using tomographic filters, and helps to illuminate one of the key uncertainties in interpreting the nature of LLSVPs. It is noteworthy that these models contain data only up to 2005, yet nevertheless have sufficient resolution to capture these features. The catalogue has expanded significantly since 2005, particularly in the

post-USArray era (Ringler *et al.* 2022), and we expect that the resolution has improved significantly since the HMSL models were constructed. Despite these increases in data coverage, some recent V_P models such as DETOX-P2 (Hosseini *et al.* 2020) and TX2019-slab (Lu *et al.* 2019) do not find slow velocities within LLSVP proportional to those observed in V_S models. This study does not address other potential concerns, such as the bias caused by many earthquakes emanating from seismically fast subduction zones (Lu *et al.* 2019), the hypothesized influence of 'wavefront healing' on the determination of P and S arrival times (Schuberth *et al.* 2009), or the influence of upper-mantle structure (Chaves *et al.* 2021). These and other questions require further study.

4.2 Temperature-only models

The tomographically filtered V_P and V_S models predicted by the T1 (temperature-only) geodynamic model are well correlated, implying that purely thermal models do not straightforwardly account for the kind of uncorrelated heterogeneity observed in the pair of HMSL models. Note that we employed a relatively simple parametrization of the effects of temperature on δV_P and δV_S, ignoring effects such as anelasticity. However, it has been suggested that anelastic effects are not sufficient to explain differences in δV_P and δV_S in the lower mantle (Hirose 2006; Brodholt *et al.* 2007). It is also possible that an electron spin crossover in ferropericlase diminishes $\partial V_P/\partial T$ relative to $\partial V_S/\partial T$ (Lin *et al.* 2013; Wu & Wentzcovitch 2014; Wang *et al.* 2021), although near the CMB these effects may be confined to the hottest regions rather than manifesting across the entire temperature range that prevails in the deepest mantle (e.g. Shephard *et al.* 2021). Nevertheless, the influence of the spin crossover is still an active area of investigation, and our understanding of these effects may evolve in the future.
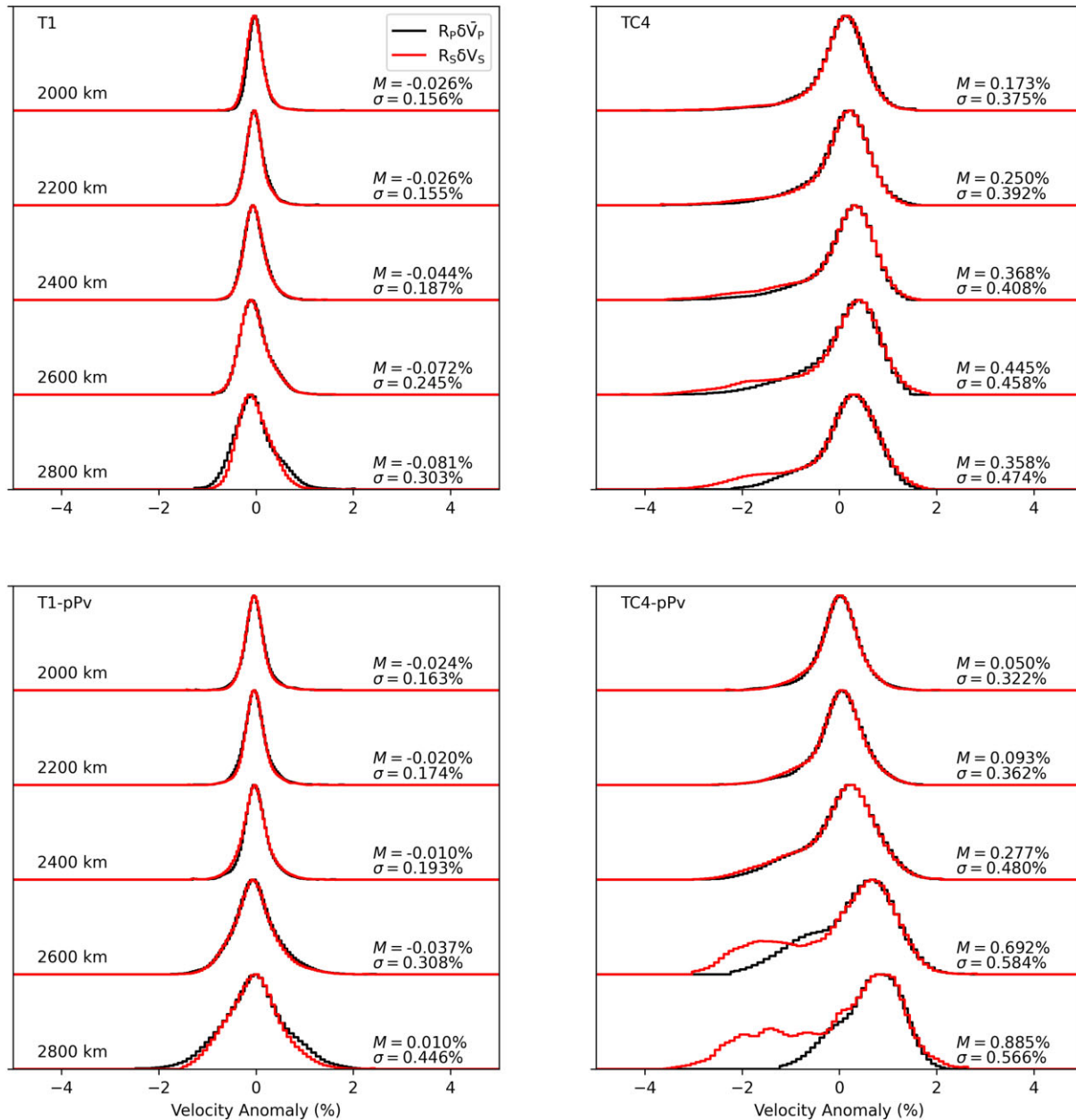
Figure 5. Distribution curves $R_P\delta\bar{V}_P$ (black) and $R_S\delta V_S$ (red) for the filtered geodynamic models from Fig. 4 at 2000, 2200, 2400, 2600 and 2800 km depth. M_S and σ_S are used to normalize filtered P model curves, which are aligned by dominant modes.

4.3 Contribution of chemical composition and/or phase variations

While the dynamic models containing chemical composition and/or phase variations do not exactly match the characteristics seen in the tomography model pair, it is clear that inclusion of these (and perhaps other) kinds of influences may help to explain uncorrelated variations in the δV_P and δV_S models. There exists a large parameter space to be explored in both the geodynamic as well as seismological parameters of these more complex models. Uncertainties in the candidate composition variations, phase stability, deep mantle temperatures, elastic parameters, in addition to transport properties that directly influence mantle dynamics need to be considered in a more general treatment before any robust conclusions can be drawn from this approach alone. Future progress on this front likely depends on relating these kinds of models to trade-offs between various hypotheses and geochemical observations.

4.4 Exploring large uncorrelated moduli provinces

We now turn to a broader exploration of the nature of uncorrelated δV_P and δV_S in the lowermost mantle, as revealed by cross-filtering. Maps of $\Delta\bar{V} = R_S\delta\bar{V}_P - R_P\delta V_S$ (Fig. 6) reveal discrepancies between δV_P and δV_S that cannot be explained by differences in resolution owing to variable coverage, and for which correlated variations have been removed by scaling and subtracting the dominant modal variations of the model pair. The distribution and sign (positive or negative) of $\Delta\bar{V} \neq 0$ material provides clues regarding the nature of the phenomena causing the δV_P–δV_S de-correlation.
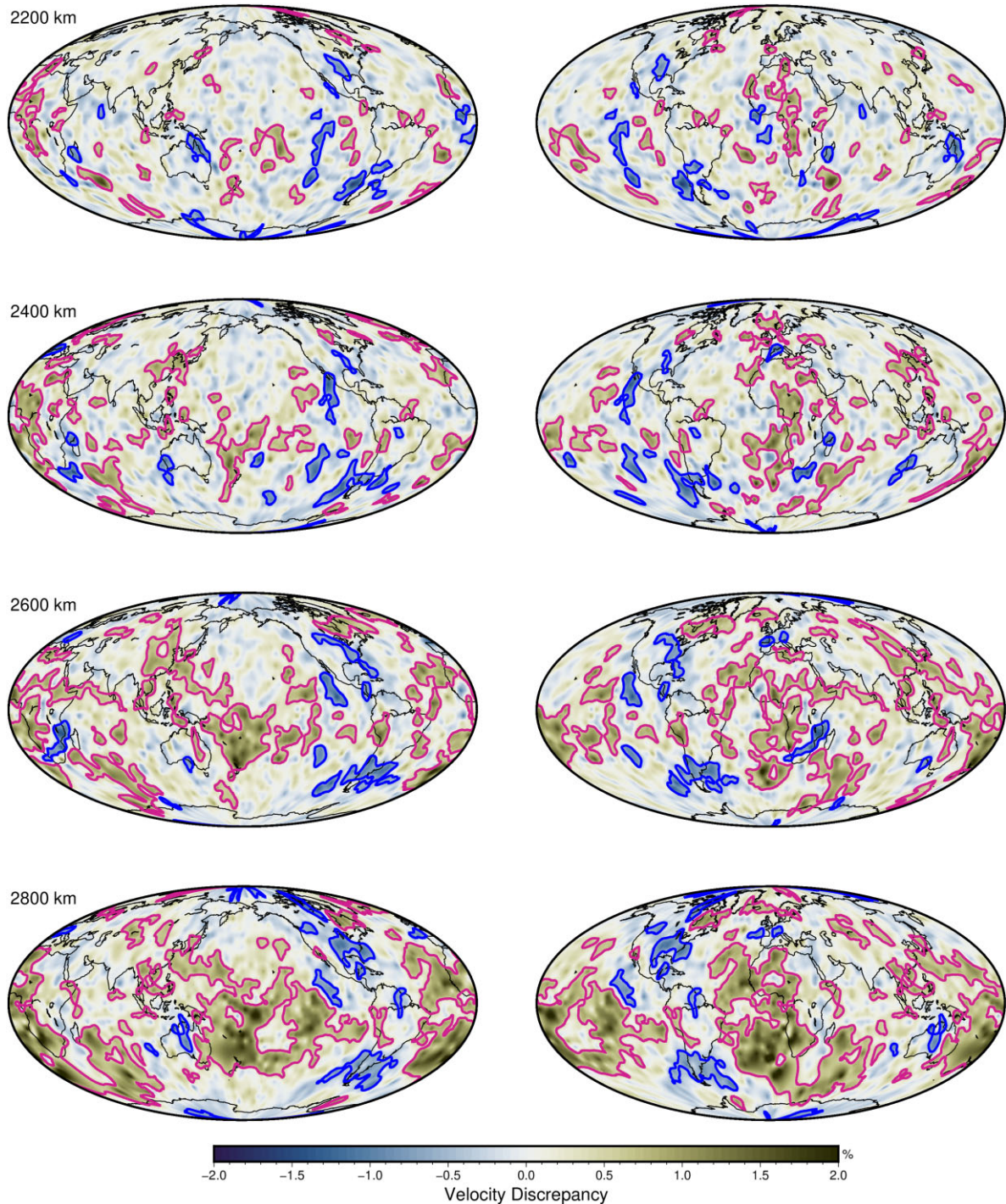
Figure 6. Maps of $\Delta\bar{V}$ and LUMPs, shown in both hemispheres (separate columns). Variations are shown using the *broc* colour map (Crameri 2021), red contoured areas show $\Delta\bar{V} > 0.5$ per cent and blue countered areas delineate $\Delta\bar{V} < -0.5$ per cent. All points with close-to-zero resolution ($R_{ii} < 10^{-3}$ for *i*th block in either *P* or *S* operator) owing to truncation are removed and, instead, interpolated to avoid overinterpretation.

The map of $\Delta\bar{V}$ reveals what we term 'large uncorrelated moduli provinces' (LUMPs). We use the term 'positive LUMP' for areas having $\Delta\bar{V} > 0.5$ per cent and 'negative lump' for those areas with $\Delta\bar{V} < -0.5$ per cent (the choice of a cut-off value of ±0.5 per cent is arbitrary, see Supporting Information S.3). In Fig. 7, we show that positive LUMPs at 2800 km depth overlap to some degree with the LLSVPs beneath Africa and the Pacific Ocean. Here, we define the edge of LLSVPs by -1 per cent velocity anomaly in the

HMSL-S06 model, similar to LLSVP boundaries across many other V_S tomography models (Lekic *et al.* 2012; Cottaar & Lekic 2016; Shephard *et al.* 2017).

Within the positive LUMPs, the change in shear modulus is more negative than the change in bulk modulus (i.e. $\delta K > \delta\mu$). A possible candidate to explain this kind of behavior is Fe-enrichment (Deschamps *et al.* 2012), which decreases shear modulus while bulk modulus is relatively unchanged, resulting in a positive value. The
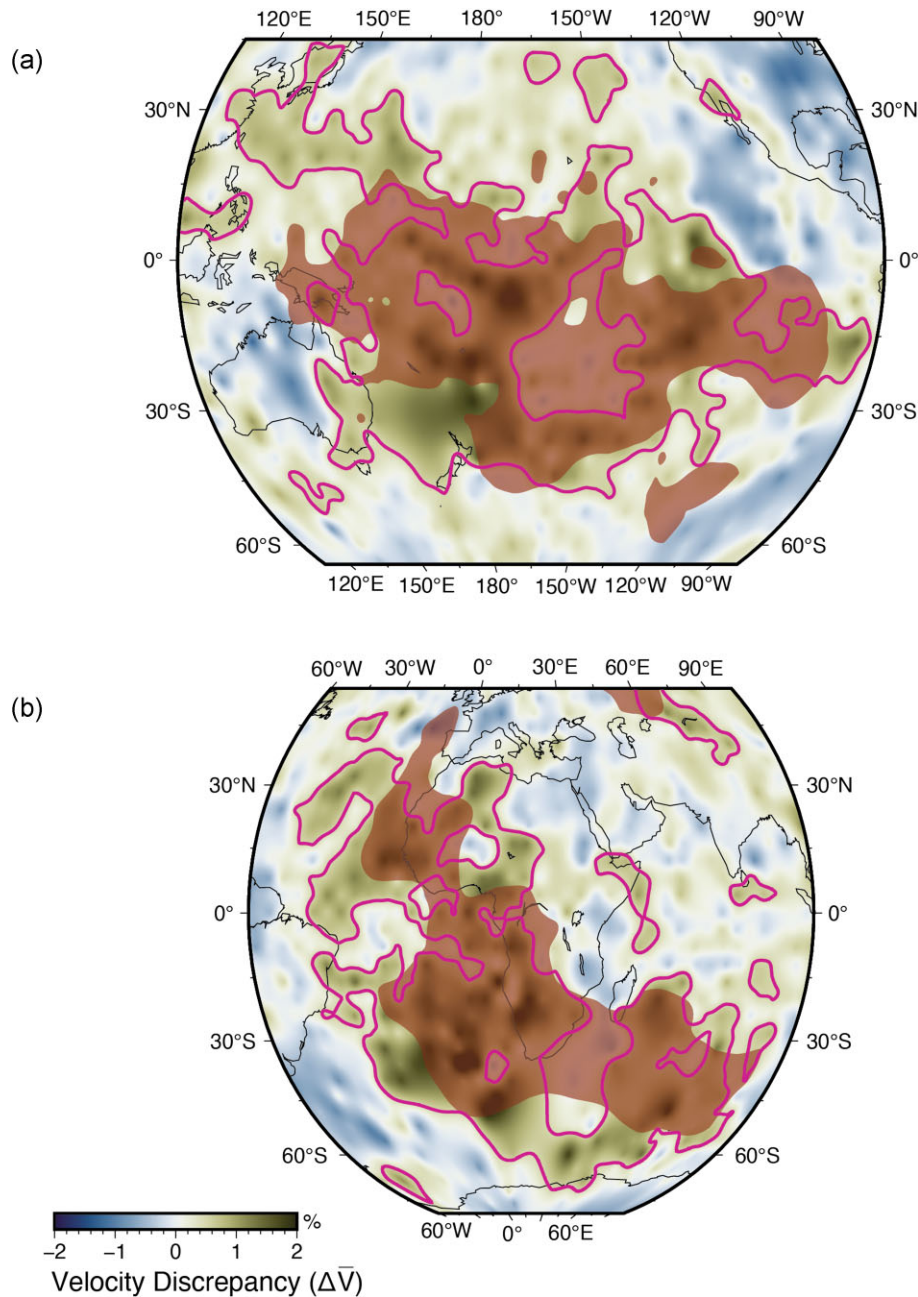
Figure 7. A comparison between conventional LLSVPs (red shade) and newly proposed positive LUMPs ($\Delta \bar{V} > 0.5$ per cent, area within bold red lines) at 2800 km depth beneath (a) the Pacific and (b) Africa. Although using an identical data set, the discrepancy map provides a unique view of lower mantle structure. LUMPs extend beyond LLSVPs, northward in the Pacific and westward in Africa, and are connected to the bulls-eye structures in the centres of these features.

extension of positive LUMPs (relative to the LLSVPs) to the north beneath the Pacific and to the west beneath Africa might suggest the presence of cooler material adjacent to the LLSVPs having the same mineralogical and/or composition change as that in LLSVPs. Note that the behaviour in the Southern Hemisphere needs to be taken with caution, owing to the relatively poor ray path coverage (for both *P* and *S*, as shown in coverage maps in Fig. 1). One can also observe the patchy structure as a characteristic of positive LUMPs, which shares some short-scale features with the LLSVPs in some recent tomography models (French & Romanowicz 2014; Mousavi *et al.* 2021). The centres of LLSVPs also exhibit a weakly positive or even negative 'bulls eye' pattern, similar to previous δV_P–δV_S

work (Hernlund & Houser 2008, fig. 4) and joint geodetic-seismic studies (e.g. Lu *et al.* 2020, fig. 10). It was previously proposed that pPv could be stabilized at high temperatures within LLSVPs by their unique Fe-rich chemical composition (Lay *et al.* 2006) or even by a pyrolite composition (Kuwayama *et al.* 2022), which might possibly explain the bulls-eye features.

Negative LUMPs, on the other hand, exhibit a change in shear modulus that is greater than changes in the bulk modulus (i.e. $\delta \mu > \delta K$). A plausible candidate to explain this behavior is the pPv phase transition (Tsuchiya *et al.* 2004) that occurs at high pressure and (relatively) low temperature conditions (Hirose 2006). There is some uncertainty regarding whether pPv is mostly confined to

the vicinity of ponded subducted slabs (e.g. Hernlund *et al.* 2005; Houser 2007) or is relatively ubiquitous everywhere in D″ outside LLSVPs (e.g. Koelemeijer *et al.* 2018). The patchy nature of the negative LUMPs seen in the present maps suggests that localized pPv may be more consistent with these seismic tomographic constraints, however, this needs further study. The spin crossover in ferropericlase (Lin *et al.* 2013; Wu & Wentzcovitch 2014; Shephard *et al.* 2021; Wang *et al.* 2021) exhibits similar properties and possibly explains the negative LUMPs above the D″ layer (e.g. 2200 and 2400 km in Fig. 6). Also note that pPv enriched regions in the tomographically filtered TC4-pPv model are only loosely recovered as negative LUMPs (see Supporting Information S.3). Future work using tomography models of higher resolution or interpretation from machine learning analysis (e.g. Rijal *et al.* 2021) will be necessary to investigate the detailed terrain and the nature of LUMPs.

5 CONCLUSIONS

In spite of the significant increase in seismic data and methodological developments in seismic tomography, there remain several significant unsettled questions about the nature and interpretation of elastic heterogeneity in the deep mantle. Tools like the tomographic filter have proven to be useful in assessing questions related to resolution, by providing a quantitative depiction of how a tomography model would 'see' hypothesized heterogeneity in the mantle. This study applied tomographic filters to a similarly constructed pair of V_P and V_S models and showed that differences in *P* and *S* coverage alone do not explain significant differences in the behaviour of δV_P and δV_S in the deep mantle. The cross-filtering approach offers a new way of exploring the nature and distribution of the several per cent of LUMPs material in the Earth's mantle, and should serve as a valuable tool for future research.

SUPPORTING INFORMATION

Supplementary data are available at *GJI* online.

Figure S1. The HMSL model in comparison to inversion δV_S (left-hand column) and δV_P (right-hand column) models obtained by SVD method for the bottom layer at 2800 km. The top row shows the HMSL-S06 model produced using the LSQR method. We construct the inversion models with the truncation factor *k*, which equals the number of vectors used at **Z**, in 6000 and 25 000.

Figure S2. Distribution curves for lowermost model layers of TC4-pPv rotated by twelve different angles before applying tomographic filters.

Figure S3. Similar to Fig. 6, but using the definition $\Delta \bar{V} = R_P \delta \bar{V}_P - R_S \delta V_S$ to measure LUMP material in T1 (left-hand column) and TC4-pPv model (right-hand column).

Please note: Oxford University Press is not responsible for the content or functionality of any supporting materials supplied by the authors. Any queries (other than missing material) should be directed to the corresponding author for the paper.

DATA AVAILABILITY

The parallel computing scripts for the SVD, reconstruction and application of resolution operators are available on GitHub (https://github.com/Jun1453/tomofilter). Due to the large file sizes, matrices for the resolution operators and sensitivity kernels of *P* and *S* model are available via a request to the corresponding author.

REFERENCES

Becker, T.W. & Boschi, L., 2002. A comparison of tomographic and geodynamic mantle models, *Geochem. Geophys. Geosyst.,* **3**(1) , doi:10.1029/2001GC000168.

Blackford, L.S. *et al.*, 1997. *ScaLAPACK users' guide,* SIAM.

Bolton, H. & Masters, G., 2001. Travel times of P and S from the global digital seismic networks: Implications for the relative variation of P and S velocity in the mantle, *J. geophys. Res. Solid Earth,* **106**(B7), 13527–13540.

Brodholt, J.P., Helffrich, G. & Trampert, J., 2007. Chemical versus thermal heterogeneity in the lower mantle: the most likely role of anelasticity, *Earth planet. Sci. Lett.,* **262**(3), 429–437.

Burke, K., Steinberger, B., Torsvik, T.H. & Smethurst, M.A., 2008. Plume generation zones at the margins of large low shear velocity provinces on the core–mantle boundary, *Earth planet. Sci. Lett.,* **265**(1), 49–60.

Chaves, C. A.M., Ritsema, J. & Koelemeijer, P., 2021. Comparing ray-theoretical and finite-frequency teleseismic traveltimes: implications for constraining the ratio of S-wave to P-wave velocity variations in the lower mantle, *Geophys. J. Int.,* **224**(3), 1540–1552.

Christensen, U.R. & Hofmann, A.W., 1994. Segregation of subducted oceanic crust in the convecting mantle, *J. geophys. Res. Solid Earth,* **99**(B10), 19867–19884.

Cottaar, S. & Lekic, V., 2016. Morphology of seismically slow lower-mantle structures, *Geophys. J. Int.,* **207**(2), 1122–1136.

Courtillot, V., 2002. *Evolutionary Catastrophes: The Science of Mass Extinction,* Cambridge University Press.

Crameri, F., 2021. *Scientific Colour Maps (7.0.1),* Zenodo,.

Davaille, A., 1999. Simultaneous generation of hotspots and superswells by convection in a heterogeneous planetary mantle, *Nature,* **402**(6763), 756–760.

Davies, D.R., Goes, S., Davies, J., Schuberth, B., Bunge, H.-P. & Ritsema, J., 2012. Reconciling dynamic and seismic models of Earth's lower mantle: the dominant role of thermal heterogeneity, *Earth planet. Sci. Lett.,* **353-354**, 253–269.

Davies, D.R., Goes, S. & Lau, H. C.P., 2015. Thermally dominated deep mantle LLSVPs: a review, in *The Earth's Heterogeneous Mantle,* pp. 441–477, Springer International Publishing.

Della Mora, S., Boschi, L., Tackley, P.J., Nakagawa, T. & Giardini, D., 2011. Low seismic resolution cannot explain S/P decorrelation in the lower mantle, *Geophys. Res. Lett.,* **38**(12) , doi:10.1029/2011GL047559.

Deschamps, F. & Li, Y., 2019. Core-mantle boundary dynamic topography: Influence of postperovskite viscosity, *J. geophys. Res. Solid Earth,* **124**(8), 9247–9264.

Deschamps, F. & Trampert, J., 2003. Mantle tomography and its relation to temperature and composition, *Phys. Earth planet. Inter.,* **140**(4), 277–291.

Deschamps, F., Cobden, L. & Tackley, P.J., 2012. The primitive nature of large low shear-wave velocity provinces, *Earth planet. Sci. Lett.,* **349-350,** 198–208.

Deschamps, F., Rogister, Y. & Tackley, P.J., 2018. Constraints on core-mantle boundary topography from models of thermal and thermochemical convection, *Geophys. J. Int.,* **212**(1), 164–188.

French, S.W. & Romanowicz, B.A., 2014. Whole-mantle radially anisotropic shear velocity structure from spectral-element waveform tomography, *Geophys. J. Int.,* **199**(3), 1303–1327.

Hassan, R., Williams, S.E., Gurnis, M. & Müller, D., 2020. East African topography and volcanism explained by a single, migrating plume, *Geosci. Front.,* **11**(5), 1669–1680.

Hernlund, J. & McNamara, A., 2015. The core-mantle boundary region, in *Treatise on Geophyiscs,* Vol. **7**, pp. 461–519, eds Schubert, G. & Bercovici, D., Elsevier.

Hernlund, J.W. & Houser, C., 2008. On the statistical distribution of seismic velocities in Earth's deep mantle, *Earth planet. Sci. Lett.,* **265**(3), 423–437.

Hernlund, J.W., Thomas, C. & Tackley, P.J., 2005. A doubling of the post-perovskite phase boundary and structure of the Earth's lowermost mantle, *Nature,* **434**(7035), 882–886.

Hirose, K., 2006. Postperovskite phase transition and its geophysical implications, *Rev. Geophys.,* **44**(3), https://doi.org/10.1029/2005RG000186.

Hosseini, K., Sigloch, K., Tsekhmistrenko, M., Zaheri, A., Nissen-Meyer, T. & Igel, H., 2020. Global mantle structure from multifrequency tomography using P, PP and P-diffracted waves, *Geophys. J. Int.,* **220**, 96–141.

Houser, C., 2007. Constraints on the presence or absence of post-perovskite in the lowermost mantle from long-period seismology, in *Post-Perovskite: The Last Mantle Phase Transition,* Vol. **174**, eds Hirose, K., Brodholt, J., Lay, T. & Yuen, D., American Geophysical Union.

Houser, C., Masters, G., Shearer, P. & Laske, G., 2008. Shear and compressional velocity models of the mantle from cluster analysis of long-period waveforms, *Geophys. J. Int.,* **174**(1), 195–212.

Hutko, A., Lay, T., Garnero, E. & Revenaugh, J.S., 2006. Seismic detection of folded, subducted lithosphere at the core-mantle boundary, *Nature,* **441**, 333–336.

Ishii, M. & Tromp, J., 1999. Normal-mode and free-air gravity constraints on lateral variations in velocity and density of Earth's mantle, *Science,* **285**(5431), 1231–1236.

Isozaki, Y., 2009. Illawarra Reversal: The fingerprint of a superplume that triggered Pangean breakup and the end-Guadalupian (Permian) mass extinction, *Gondwana Res.,* **15**(3), 421–432.

Jellinek, A.M. & Manga, M., 2004. Links between long-lived hot spots, mantle plumes, D″, and plate tectonics, *Rev. Geophys.,* **42**(3) , doi:10.1029/2003RG000144.

Jones, T.D., Maguire, R.R., van Keken, P.E., Ritsema, J. & Koelemeijer, P., 2020. Subducted oceanic crust as the origin of seismically slow lower-mantle structures, *Prog. Earth Planet. Sci.,* **7**(1) , doi:10.1186/s40645-020-00327-1.

Jones, T.D., Sime, N. & van Keken, P.E., 2021. Burying Earth's primitive mantle in the slab graveyard, *Geochem. Geophys. Geosyst.,* **22**(3), e2020GC009396 , doi:10.1029/2020GC009396.

Karato, S.-I. & Karki, B.B., 2001. Origin of lateral variation of seismic wave velocities and density in the deep mantle, *J. geophys. Res. Solid Earth,* **106**(B10), 21771–21783.

Kellogg, L.H., Hager, B.H. & van der Hilst, R.D., 1999. Compositional stratification in the deep mantle, *Science,* **283**(5409), 1881–1884.

Koelemeijer, P., Ritsema, J., Deuss, A. & van Heijst, H.-J., 2016. SP12RTS: a degree-12 model of shear- and compressional-wave velocity for Earth's mantle, *Geophys. J. Int.,* **204**(2), 1024–1039.

Koelemeijer, P., Schuberth, B., Davies, D., Deuss, A. & Ritsema, J., 2018. Constraints on the presence of post-perovskite in Earth's lowermost mantle from tomographic-geodynamic model comparisons, *Earth planet. Sci. Lett.,* **494**, 226–238.

Kuwayama, Y., Hirose, K., Cobden, L., Kusakabe, M., Tateno, S. & Ohishi, Y., 2022. Post-erovskite phase transition in the pyrolitic lowermost mantle: implications for ubiquitous occurrence of post-perovskite above CMB, *Geophys. Res. Lett.,* **49**(1), e2021GL096219, https://doi.org/10.1029/2021GL096219.

Labrosse, S., Hernlund, J.W. & Coltice, N., 2007. A crystallizing dense magma ocean at the base of the Earth's mantle, *Nature,* **450**(7171), 866–869.

Lay, T., Hernlund, J., Garnero, E. & Thorne, M., 2006. A post-perovskite lens and D″ heat flux beneath the central Pacific, *Science,* **314**(5803), 1272–1276.

Lei, W. *et al.*, 2020. Global adjoint tomography—model GLAD-M25, *Geophys. J. Int.,* **223**, 1–21.

Lekic, V., Cottaar, S., Dziewonski, A. & Romanowicz, B., 2012. Cluster analysis of global lower mantle tomography: a new class of structure and implications for chemical heterogeneity, *Earth planet. Sci. Lett.,* **357-358**, 68–77.

Li, Y., Deschamps, F. & Tackley, P., 2016. Small post-perovskite patches at the base of lower mantle primordial reservoirs: Insights from 2-D numerical modeling and implications for ULVZs, *Geophys. Res. Lett.,* **43**, 3215–3225.

Lin, J.-F., Speziale, S., Mao, Z. & Marquardt, H., 2013. Effects of the electronic spin transitions of iron in lower mantle minerals: implications for deep mantle geophysics and geochemistry, *Rev. Geophys.,* **51**, 244–275.

Lu, C., Grand, S.P., Lai, H. & Garnero, E.J., 2019. TX2019slab: a new P and S tomography model incorporating subducting slabs, *J. geophys. Res. Solid Earth,* **124**(11), 11549–11567.

Lu, C., Forte, A.M., Simmons, N.A., Grand, S.P., Kajan, M.N., Lai, H. & Garnero, E.J., 2020. The sensitivity of joint inversions of seismic and geodynamic data to mantle viscosity, *Geochem. Geophys. Geosyst.,* **21**(4), e2019GC008648 , doi:10.1029/2019GC008648.

Malcolm, A.E. & Trampert, J., 2011. Tomographic errors from wave front healing: more than just a fast bias, *Geophys. J. Int.,* **185**(1), 385–402.

Maruyama, S., Santosh, M. & Zhao, D., 2007. Superplume, supercontinent, and post-perovskite: mantle dynamics and anti-plate tectonics on the core–mantle boundary, *Gondwana Res.,* **11**(1), 7–37.

Matyska, C., Moser, J. & Yuen, D.A., 1994. The potential influence of radiative heat transfer on the formation of megaplumes in the lower mantle, *Earth planet. Sci. Lett.,* **125**(1), 255–266.

McNamara, A.K. & Zhong, S., 2005. Thermochemical structures beneath Africa and the Pacific Ocean, *Nature,* **437**(7062), 1136–1139.

Moulik, P. & Ekström, G., 2016. The relationships between large-scale variations in shear velocity, density, and compressional velocity in the Earth's mantle, *J. geophys. Res. Solid Earth,* **121**(4), 2737–2771.

Mousavi, S., Tkalčić, H., Hawkins, R. & Sambridge, M., 2021. Lowermost mantle shear-velocity structure from hierarchical trans-dimensional Bayesian tomography, *J. geophys. Res. Solid Earth,* **126**(9), e2020JB021557 , doi:10.1029/2020JB021557.

Nakagawa, T., Tackley, P.J., Deschamps, F. & Connolly, J. A.D., 2009. Incorporating self-consistently calculated mineral physics into thermochemical mantle convection simulations in a 3-D spherical shell and its influence on seismic anomalies in Earth's mantle, *Geochem. Geophys. Geosyst.,* **10**(3) , doi:10.1029/2008GC002280.

Ohta, K., Hirose, K., Lay, T., Sata, N. & Ohishi, Y., 2008. Phase transitions in pyrolite and MORB at lowermost mantle conditions: implications for a MORB-rich pile above the core–mantle boundary, *Earth planet. Sci. Lett.,* **267**(1), 107–117.

Richards, M.A., Duncan, R.A. & Courtillot, V.E., 1989. Flood basalts and hot-spot tracks: plume heads and tails, *Science,* **246**(4926), 103–107.

Rijal, A., Cobden, L., Trampert, J., Jackson, J.M. & Valentine, A., 2021. Inferring material properties of the lower mantle minerals using mixture density networks, *Phys. Earth planet. Inter.,* **319**, 106784 , doi:10.1016/j.pepi.2021.106784.

Ringler, A. *et al.*, 2022. Achievements and prospects of global broadband seismographic networks after 30 years of continuous geophysical observations, *Rev. Geophys.,* **60**, e2021RG000749 , doi:10.1029/2021RG000749.

Ritsema, J., McNamara, A.K. & Bull, A.L., 2007. Tomographic filtering of geodynamic models: Implications for model interpretation and large-scale mantle structure, *J. geophys. Res. Solid Earth,* **112**(B1) , doi:10.1029/2006JB004566.

Schuberth, B. S.A., Bunge, H.-P. & Ritsema, J., 2009. Tomographic filtering of high-resolution mantle circulation models: can seismic heterogeneity be explained by temperature alone?, *Geochem. Geophys. Geosyst.,* **10**(5), https://doi.org/10.1029/2009GC002401.

Shephard, G.E., Matthews, K.J., Hosseini, K. & Domeier, M., 2017. On the consistency of seismically imaged lower mantle slabs, *Sci. Rep.,* **7**(1) , doi:10.1038/s41598-017-11039-w.

Shephard, G.E., Houser, C., Hernlund, J.W., Valencia-Cardona, J.J., Trønnes, R.G. & Wentzcovitch, R.M., 2021. Seismological expression of the iron spin crossover in ferropericlase in the Earth's lower mantle, *Nat. Commun.,* **12**(1) , doi:10.1038/s41467-021-26115-z.

Simmons, N., Forte, A. & Grand, S., 2007. Thermochemical structure and dynamics of the African superplume, *Geophys. Res. Lett.,* **34**, L02301 , doi:10.1029/2006GL028009.

Simmons, N.A., Forte, A.M., Boschi, L. & Grand, S.P., 2010. GyPSuM: A joint tomographic model of mantle density and seismic wave speeds, *J. geophys. Res. Solid Earth,* **115**(B12) , doi:10.1029/2010JB007631.

Simmons, N.A., Schuberth, B. S.A., Myers, S.C. & Knapp, D.R., 2019. Resolution and covariance of the LLNL-G3D-JPS global seismic tomography model: applications to travel time uncertainty and tomographic filtering of geodynamic models, *Geophys. J. Int.,* **217**(3), 1543–1557.

Stackhouse, S., Brodholt, J.P., Dobson, D.P. & Price, G.D., 2006. Electronic spin transitions and the seismic properties of ferrous iron-bearing MgSiO3 post-perovskite, *Geophys. Res. Lett.,* **33**(12) , doi:10.1029/2005GL025589.

Tackley, P.J., 2011. Living dead slabs in 3-D: The dynamics of compositionally-stratified slabs entering a "slab graveyard" above the core-mantle boundary, *Phys. Earth planet. Inter.,* **188**(3), 150–162.

Tan, E. & Gurnis, M., 2007. Compressible thermochemical convection and application to lower mantle structures, *J. geophys. Res. Solid Earth,* **112**(B6) , doi:10.1029/2006JB004505.

Tesoniero, A., Cammarano, F. & Boschi, L., 2016. S–to–P heterogeneity ratio in the lower mantle and thermo-chemical implications, *Geochem. Geophys. Geosyst.,* **17**(7), 2522–2538.

Thompson, P.F. & Tackley, P.J., 1998. Generation of mega-plumes from the core-mantle boundary in a compressible mantle with temperature-dependent viscosity, *Geophys. Res. Lett.,* **25**(11), 1999–2002.

Trampert, J., Deschamps, F., Resovsky, J. & Yuen, D., 2004. Probabilistic tomography maps chemical heterogeneities throughout the lower mantle, *Science,* **306**(5697), 853–856.

Trønnes, R., Baron, M., Eigenmann, K., Guren, M., Heyn, B., Løken, A. & Mohn, C., 2019. Core formation, mantle differentiation and core-mantle interaction within Earth and the terrestrial planets, *Tectonophysics,* **760**, 165–198.

Trønnes, R.G., 2009. Structure, mineralogy and dynamics of the lowermost mantle, *Mineral. Petrol.,* **99**(3–4), 243–261.

Tsuchiya, T., Tsuchiya, J., Umemoto, K. & Wentzcovitch, R.M., 2004. Elasticity of post-perovskite MgSiO3, *Geophys. Res. Lett.,* **31**(14) , doi:10.1029/2004GL020278.

Walter, M.J. & Trønnes, R.G., 2004. Early earth differentiation, *Earth planet. Sci. Lett.,* **225**(3), 253–269.

Wang, W., Liu, J., Zhu, F., Li, M., Dorfman, S.M., Li, J. & Wu, Z., 2021. Formation of large low shear velocity provinces through the decomposition of oxidized mantle, *Nat. Commun.,* **12**(1) , doi:10.1038/s41467-021-22185-1.

Wang, X.-C., Li, Z.-X. & Li, X.-H., 2013. Early differentiation of the bulk silicate Earth as recorded by the oldest mantle reservoir, *Precambrian Res.,* **238**, 52–60.

Wu, Z. & Wentzcovitch, R., 2014. Spin crossover in ferropericlase and velocity heterogeneities in the lower mantle, *Proc. Nat. Acad. Sci.,* **111**, 10468–10472.

Yanagisawa, T. & Hamano, Y., 1999. "Skewness" of S-wave velocity in the mantle, *Geophys. Res. Lett.,* **26**(6), 791–794.